

Filament-Based Atmospheric Dispersion Model to Achieve Short Time-Scale Structure of Odor Plumes

Jay A. Farrell

Department of Electrical Engineering, University of California, Riverside

John Murlis and Xuezhu Long

School of Public Policy, University College London

Wei Li

Department of Computer Science, California State University, Bakersfield

Ring Cardé

Department of Entomology, University of California, Riverside

Abstract. This article presents the theoretical motivation, implementation approach, and example validation results for a computationally efficient plume simulation model, designed to replicate both the short-term time signature and long-term exposure statistics of a chemical plume evolving in a turbulent flow. Within the resulting plume, the odor concentration is intermittent with rapidly changing spatial gradient. The model includes a wind field defined over the region of interest that is continuous, but which varies with location and time in both magnitude and direction. The plume shape takes a time varying sinuous form that is determined by the integrated effect of the wind field. Simulated and field data are compared. The motivation for the development of such a simulation model was the desire to evaluate various strategies for tracing odor plumes to their source, under identical conditions. The performance of such strategies depends in part on the instantaneous response of target receptors; therefore, the sequence of events is of considerable consequence and individual exemplar plume realizations are required. Due to the high number of required simulations, computational efficiency was critically important.

Keywords: Chemical Plume Tracing, Odor Dispersion Model, Pheromone Dispersion

Running title: Dispersion model with meander and concentration fluctuations

20020322 159

⁰ Corresponding author. Jay A. Farrell, Department of Electrical Engineering, A220 Bourns Hall, University of California, Riverside 92506 USA; e-mail: farrell@ee.ucr.edu; v: 909-787-2423; f: 909-787-2425.



© 2002 Kluwer Academic Publishers. Printed in the Netherlands.

1. Introduction

Olfactory-based mechanisms have been used to explain a variety of biological orientation behaviors for resource location [1, 2, 3, 4]: homing by Pacific salmon [5] and green sea turtles [6]; foraging by Antarctic procellariiform seabirds [7], lobsters [8, 9, 10], and blue crabs [11]; and mate finding and foraging by insects [12, 13, 14]. Typically, olfactory-based mechanisms proposed for biological entities combine orientation behaviors at long-range based in part on olfaction with a local search in the vicinity of the source governed by multiple sensor modalities. The olfactory portion of the search strategy is contingent on the fact that a turbulent flow can transport above threshold parcels of odor over relatively long distances, making feasible the detection of an upflow odor emitter over considerable distances. A further advantage to the searcher is that the odor signal can be highly specific, resulting in rare false positive responses [15]. The flight of a male moth along a wind-dispersed plume of pheromone, emitted either by a female or a dispenser charged with synthetic pheromone is particularly well-documented [12, 16, 17, 18, 19, 20]. Models of moth navigation generally propose that males fly upwind when they sense an above-threshold concentration of pheromone. This mechanism is termed 'positive anemotaxis.' Because in a rapidly-flying insect, navigational decisions require continual review of the sensor by the insect, the fine-scale plume structure is of considerable consequence.

The fact that various biological entities use olfactory based search with high degrees of success has prompted research¹ into the design of autonomous vehicles capable of olfactory based search and chemical plume tracing. Such autonomous vehicle capabilities have applicability in searching for environmentally interesting phenomena, hazardous chemicals, and pollutants. In addition to vehicle development, sensor development, and analysis of the fluid environment, design and optimization of the chemical plume tracing (CPT) strategies are of critical importance to the solution of this problem. Evaluation of CPT strategies requires hardware and software evaluation platforms. During the initial design stages, software evaluation is preferred, since such tools allow competing strategies to be evaluated under identical conditions for various environmental scenarios. The tradeoffs between field testing, wind tunnel testing, and simulation testing are discussed in, for example, [33, 34]. To calculate reliable performance statistics, numerous² batches of such evaluations are required. Therefore, the computational efficiency of the software simulation tools is a key concern. To ensure that strategies that perform well in simulation will also perform well in hardware experiments, the

simulation must contain the key features that complicate the problem of CPT. This article presents a plume simulation implementation that addresses the tradeoffs between computational efficiency and inclusion of realistic complicating features.

Plume models can represent concentration by its mean or probability density function. For example, dispersion in a turbulent medium is frequently represented as a Gaussian distribution such as [21, 22, 23, 24]

$$\bar{C}(x, y, z) = \frac{Q}{2\pi S_y S_z \bar{u}} \exp \left(- \left(\frac{y^2}{2S_y^2} + \frac{z^2}{2S_z^2} \right) \right) \quad (1)$$

where $\bar{C}(x, y, z)$ represents the average concentration profile as a function of position. In this expression, and throughout this article, x, y, and z denote the downwind, crosswind, and vertical position coordinates relative to the odor source with x positive along the mean wind direction. S_y and S_z are the standard deviations of the time-averaged plume concentration in the crosswind and vertical directions. Both parameters are functions of the downwind position. The parameters of the functional fit may be based on theoretical considerations (i.e., $S_y = 0.5C_y x^{(2-n)/2}$ and $S_z = 0.5C_z x^{(2-n)/2}$) [23, 24] or selected to match experimental data for the atmospheric conditions of interest [22, 25, 26]. The application of Gaussian plume concentration models is well established and the results they produce are well understood. Predictions based on Gaussian plume studies yield results that match experimental results reasonably well when long-term exposure is of interest and the effect of the exposure is a linear function of the time averaged concentration [27]. Probability density plume models, however, do not set out to provide information related to the short time-scale signature of the concentration, the instantaneous peak concentration, or the intermittent nature of the plume. Although the fine-scale characteristics of a plume are of little interest in many cases, for example in some kinds of regulatory work related to permitting or safety, they are of considerable importance in others, for example in assessing flammability and the health impacts of toxic release, in studies of biological response to odor [14, 28], and pollution damage to plants [29]. Because behavioral reactions are governed by instantaneous or nearly instantaneous concentrations of odor [30] and such probability density estimates cannot be used to accurately predict where in space an odor is instantaneously above threshold, probability density plume models are not appropriate for the CPT strategy performance analysis.

This article presents a model for dispersion in a turbulent medium. The specific purpose of this plume dispersion model is to facilitate modeling and analysis of navigation strategies designed

to locate a wind-dispersed odor plume and then to trace it to its source³. It is well known (e.g., [31, 32]) that direct numeric simulation (DNS) of turbulent flow in reasonable amounts of time is limited by computational power to large grid size or low Reynolds numbers. Therefore, this article presents the design of a simplified plume simulation, based on physical principles, that resulted in a computationally feasible simulation (i.e., 100 batches of 100 source relative starting locations evaluated on a 100 by 100 m area in less than 24 hours on a typical desktop computer). The simulation design presented herein addresses the following tradeoffs:

1. Field studies have shown that odor detection events can have pulse widths on the order of 0.01s [27]. Moths have been shown to respond to odorant pulse widths on the order of 0.1 s [14]. Therefore, the fine-time scale structure of the sensed odor is important.
2. Although the fine structure of the turbulent flow is important in the process of transporting relatively undiluted parcels of odor over long distances, the anticipated vehicle flow sensors will be unable to resolve the fine-scale flow structure. Therefore, accurate simulation of the fine-scale flow itself is not important.
3. The plume must have an intermittent internal structure in the sense that a snapshot of the plume appears as patches of above threshold odor.
4. The sinuous (or meandering) nature of the plume is a key complicating factor to plume tracking. The simulation must generate plumes that meander. In addition, the meander should be coherent with the flow field in the sense that the odor distribution down wind from the source is the result of advection by the flow field.
5. The simulation must generate exemplar plumes, not time-averaged odor distributions. The simulation should be capable of returning measured concentration at location $x(t)$ at time t . Both position and time will change as the searcher executes its mission. The searcher trajectory will respond to the sensed flow and odor detection events. This searcher trajectory cannot be predicted prior to the simulation. Therefore, the simulation must maintain models of the flow and odor concentration as a function of position and time.
6. The effect of the searcher on the flow and the odor distribution are not considered important for this application, because the searcher, which is trying to make progress up the plume,

mainly affects the downwind flow and odor distribution. Inclusion of these effects would significantly increase the computational burden without significantly affecting the strategy evaluation results.

The goal of the simulation discussed herein is, therefore, to produce a more challenging and physically plausible simulation model than those currently used in insect behavioral and robotic strategy design studies, e.g., [34, 33, 35, 36], while achieving significant computational simplification relative to the turbulence simulation models in the literature, e.g., [37, 38, 39, 40, 41, 32].

1.1. ARTICLE OVERVIEW

To generate realistic simulated plumes we considered the following three characteristic structural features to be of primary concern. First, the sensed plume at a fixed location should have an intermittent internal structure that closely duplicates experimental observations. Second, the plume that results from a semi-continuous release of odor should be sinuous and time varying. Third, the plume shape and wind field history should be coherent.

The first characteristic feature is achieved herein by representing the odor plume as a sequence of puffs [33, 55]. Puffs are released sequentially at the source location. Each puff is composed of n filaments. After release, the filament center location is determined by integration of the wind velocity:

$$\dot{\mathbf{p}}_i = \mathbf{v}(\mathbf{p}_i) \quad (2)$$

where \mathbf{p}_i and $\mathbf{v}(\mathbf{p}_i)$ are the 3 dimensional position of the i -th filament and wind velocity at the location of the i -th filament. To achieve the second characteristic feature, our model incorporates a dynamic model of the wind. This model allows the wind, which transports the filaments, to be a continuous but varying function of position and time. Changes in wind direction cause the plume to meander (form a snake-like path when viewed from above). As the wind velocity changes, the instantaneous wind direction at given positions within the plume's boundaries sometimes will not point either toward the odor's source nor be coincident with the direction of the plume's centerline. These characteristics of the simulated plume reproduce experimentally observed phenomena [42, 43].

The puff-based model presented here is general and is designed so that it can be tuned for a range of applications. For the simulation results presented here, the parameters were tuned to correspond

to odor plumes as perceived by male moths. The receptor system of some male moths is capable of resolving 10 odor pulses per second [44]. A flying male can react to odor filaments of 200 ms duration [14, 45]. Therefore, we designed the present model of plume dispersion with an integration time step of 10 ms. Similarly, the units of the sensed odor (see Section 2.4) were specified to be relevant to the male moth.

Conventional time-averaged concentration models are in general time independent. It is assumed that the plume was fully developed prior to the initiation of data collection. Such concentration distributions (assuming stationarity and ergodicity) allow time independent predictions *over an ensemble* of plumes of the average concentration as a function of position. Measured instantaneous concentration of specific exemplar plumes can, however, deviate significantly from the ensemble average [27, 46, 47, 48]. Alternatively, instantaneous concentrations as produced by simulation models produce a model instance of an odor plume as an individual realization. By design, such a plume will be time varying; however, when time averaged, the mean concentration should match the above ensemble averages. In addition, simulated plume models enable certain types of analysis that are precluded by the loss of time signature information in mean concentration plume models, such as analysis of alternative biological strategies under uniform experimental conditions (see e.g., [34, 33]).

The objective of this article is to present a simulation model for an odor plume that (1) realistically reproduces the short time-scale signature for sensed concentrations, (2) accurately reproduces the long-term time-averaged plume data, (3) incorporates a simulated wind (advection) model that is continuous over a region of interest but time varying in magnitude and direction, and (4) is computable in reasonable time. The presentation of the model is followed by analysis of simulated results in relation to experimental results previously reported in the literature.

2. Model Overview

A chemical released at a source location will be manipulated by turbulent and molecular diffusion while transported advectively by the wind. As described in [46, 49], the odor dispersion process is dominated by turbulent dispersion. Turbulent dispersion involves a wide range of length (or eddy) scales. Eddies larger than the scale of a section of the plume (i.e., a puff) transport the puff as a

whole, causing the ensemble of puffs to appear as a sinuous plume. Eddies smaller than the puff mix the components of the puff causing little puff motion or growth. Eddies on the order of the puff size cause significant growth/distortion of the puff and motion of individual filaments relative to the instantaneous plume centerline.

To develop a corresponding plume simulation model, the velocity vector will be decomposed into three components: \mathbf{v}_d , \mathbf{v}_m , and \mathbf{v}_a . Each component will be implemented by a distinct process as described in the subsequent sections. This decomposition of the velocity spectrum is motivated by the numerical implementation, but can be interpreted theoretically in terms of the eddy scales of the previous paragraph. To clarify this correspondence, it is first necessary to state that the puffs, for simulation, will be further decomposed into parcels referred to herein as *filaments*. The effect of the smallest eddies (i.e., slow growth of the filaments) of the wind fluid flow process (modeled by \mathbf{v}_d) will be implemented as an increase in filament size and change in shape, as described in Section 2.3. The term \mathbf{v}_a represents the portion of the wind process with characteristic length much larger than the filaments. This portion of the wind process transports each filament as a body; therefore, the term \mathbf{v}_a represents advection. The advection portion of the velocity is represented as a continuous (in time and space), but temporally and spatially varying function (see Section 2.1), so that a sequence of filaments released at the source will result in a sinuous trail of filaments leaving the source. The term \mathbf{v}_m represents the intermediate range of scales that transports (i.e., stirs) the filaments within the body of the plume.

Although the position of individual molecules cannot be conveniently simulated, the idea is useful to consider for the purpose of defining the simulation. Therefore, the position of a single molecule is given by

$$\dot{\mathbf{p}}_m = \mathbf{v}_d + \mathbf{v}_m + \mathbf{v}_a. \quad (3)$$

Because the intermediate and advective terms affect all molecules within a filament similarly, the model can be decomposed into two processes—the changing shape of the filament and the transport of the filament. The position of the i -th filament will be represented by \mathbf{p}_i . The changing position of the i -th filament is represented by

$$\dot{\mathbf{p}}_i = \mathbf{v}_{m_i} + \mathbf{v}_a. \quad (4)$$

where the implementation of the \mathbf{v}_{m_i} and \mathbf{v}_a processes is discussed in subsequent sections.

Physically, the growing and changing shape of the filament is a very interesting process dominated by turbulent diffusion. However, numerical simulation of diffusion processes is a complex and (simulation) time consuming task. Therefore, at this level some compromise is required to achieve reasonable simulation times while still achieving the objectives of the simulation model. The approach herein is to use a template filament shape that can change size and orientation. The simulation results are not sensitive to the choice of template shape, as long as the change in shape is physically reasonable.

Any numeric flow simulation must satisfy various conservation equations (see Ch. 2 in [39]). For the simulation herein, conservation of the mass of the flowing material and conservation of momentum is addressed in Sections 2.1 and 2.2. Conservation of the mass of the odor is addressed through the filament representation as described in Section 2.3.

2.1. ADVECTION

This section describes the theoretical model for $\mathbf{v}_a = (\bar{u}, \bar{v}, \bar{w})$ suitable for simulation implementation. The advection model is currently implemented in two dimensions (i.e., x and y) with the assumption that for the area of interest \mathbf{v}_a is independent of z . This assumption is motivated by the assumption that the plume tracing will occur at a nearly constant altitude within a few meters of the ocean floor or earth surface. Issues related to plume dispersion in a stratified flow are discussed in [50].

Within the atmospheric surface layer, we have assumed that compared with turbulent forces, the following forces on an air parcel are negligible: Coriolis, geostrophic winds, and molecular viscosity. It is also assumed that time-averaged pressure terms can be neglected, so that the time-mean motion equations are

$$\begin{aligned} \frac{\partial \bar{u}}{\partial t} &= -\bar{u} \frac{\partial \bar{u}}{\partial x} - \bar{v} \frac{\partial \bar{u}}{\partial y} - \bar{w} \frac{\partial \bar{u}}{\partial z} \\ &\quad - \frac{\partial \bar{u}'u'}{\partial x} - \frac{\partial \bar{u}'v'}{\partial y} - \frac{\partial \bar{u}'w'}{\partial z} \end{aligned} \quad (5)$$

$$\begin{aligned} \frac{\partial \bar{v}}{\partial t} &= -\bar{u} \frac{\partial \bar{v}}{\partial x} - \bar{v} \frac{\partial \bar{v}}{\partial y} - \bar{w} \frac{\partial \bar{v}}{\partial z} \\ &\quad - \frac{\partial \bar{v}'u'}{\partial x} - \frac{\partial \bar{v}'v'}{\partial y} - \frac{\partial \bar{v}'w'}{\partial z} \end{aligned} \quad (6)$$

with the continuity equation

$$0 = \frac{\partial \bar{u}}{\partial x} + \frac{\partial \bar{v}}{\partial y} + \frac{\partial \bar{w}}{\partial z} \quad (7)$$

where $u(t) = \bar{u}(t) + u'(t)$. To conserve computational resources we have used the simplest form of K-closure method [51, 39] under the assumption, applicable under near neutral conditions, that

$$\overline{u' u'} = -K_x \frac{\partial \bar{u}}{\partial x} \quad \overline{v' v'} = -K_y \frac{\partial \bar{v}}{\partial y} \quad (8)$$

$$\overline{u' w'} = -K_z \frac{\partial \bar{u}}{\partial z} \quad \overline{v' w'} = -K_z \frac{\partial \bar{v}}{\partial z}, \quad (9)$$

and

$$\overline{u' v'} = \overline{v' u'} = -\frac{1}{2} \left(K_x \frac{\partial \bar{v}}{\partial x} + K_y \frac{\partial \bar{u}}{\partial y} \right) \quad (10)$$

where the K_x , K_y , and K_z terms represent diffusivity. Assuming that, for the region of the plume with which we are concerned (approximately a hundred meters in length), turbulence is homogeneous and approximately isotropic,

$$K_x = K_y \quad (11)$$

$$0 = \frac{\partial K_x}{\partial x} = \frac{\partial K_y}{\partial y} = \frac{\partial K_z}{\partial z}. \quad (12)$$

Note that the K_x , K_y , and K_z terms could be assumed to be appropriate functions of position at minimal computational cost, with appropriate changes in eqns. (11-12). In the present simulation, $K_x \in [1, 30] \frac{m^2}{s}$ is a constant. Under these assumptions, the dynamic wind (advection) model for the u -term simplifies as follows

$$\begin{aligned} \frac{\partial \bar{u}}{\partial t} &= -\bar{u} \frac{\partial \bar{u}}{\partial x} - \bar{v} \frac{\partial \bar{u}}{\partial y} - \bar{w} \frac{\partial \bar{u}}{\partial z} \\ &\quad + K_x \frac{\partial^2 \bar{u}}{\partial x^2} + \frac{1}{2} K_y \frac{\partial}{\partial y} \left(\frac{\partial \bar{u}}{\partial y} + \frac{\partial \bar{v}}{\partial x} \right) + K_z \frac{\partial^2 \bar{u}}{\partial z^2} \end{aligned} \quad (13)$$

$$\begin{aligned} &= -\bar{u} \frac{\partial \bar{u}}{\partial x} - \bar{v} \frac{\partial \bar{u}}{\partial y} - \bar{w} \frac{\partial \bar{u}}{\partial z} \\ &\quad + \frac{1}{2} K_x \frac{\partial^2 \bar{u}}{\partial x^2} + \frac{1}{2} K_x \frac{\partial^2 \bar{u}}{\partial y^2} + \frac{1}{2} K_x \left(\frac{\partial^2 \bar{u}}{\partial x^2} + \frac{\partial^2 \bar{v}}{\partial y \partial x} \right) + K_z \frac{\partial^2 \bar{u}}{\partial z^2} \end{aligned} \quad (14)$$

$$\begin{aligned} &= -\bar{u} \frac{\partial \bar{u}}{\partial x} - \bar{v} \frac{\partial \bar{u}}{\partial y} - \bar{w} \frac{\partial \bar{u}}{\partial z} \\ &\quad + \frac{1}{2} K_x \frac{\partial^2 \bar{u}}{\partial x^2} + \frac{1}{2} K_x \frac{\partial^2 \bar{u}}{\partial y^2} + \frac{1}{2} K_x \frac{\partial}{\partial x} \left(\frac{\partial \bar{u}}{\partial x} + \frac{\partial \bar{v}}{\partial y} \right) + K_z \frac{\partial^2 \bar{u}}{\partial z^2} \end{aligned} \quad (15)$$

$$\begin{aligned} &= -\bar{u} \frac{\partial \bar{u}}{\partial x} - \bar{v} \frac{\partial \bar{u}}{\partial y} - \bar{w} \frac{\partial \bar{u}}{\partial z} \\ &\quad + \frac{1}{2} K_x \frac{\partial^2 \bar{u}}{\partial x^2} + \frac{1}{2} K_x \frac{\partial^2 \bar{u}}{\partial y^2} - \frac{1}{2} K_x \frac{\partial}{\partial x} \left(\frac{\partial \bar{w}}{\partial z} \right) + K_z \frac{\partial^2 \bar{u}}{\partial z^2} \end{aligned} \quad (16)$$

The model for \bar{v} can be processed similarly. If it is assumed that the model is applied in a narrow layer near the surface of the earth, on a region where $\mathbf{v}_a = (\bar{u}, \bar{v}, \bar{w})$ is independent of z , then the following simplified two dimensional model results:

$$\begin{aligned}\frac{\partial \bar{u}}{\partial t} &= -\bar{u} \frac{\partial \bar{u}}{\partial x} - \bar{v} \frac{\partial \bar{u}}{\partial y} \\ &+ \frac{1}{2} K_x \frac{\partial^2 \bar{u}}{\partial x^2} + \frac{1}{2} K_x \frac{\partial^2 \bar{u}}{\partial y^2}\end{aligned}\quad (17)$$

$$\begin{aligned}\frac{\partial \bar{v}}{\partial t} &= -\bar{u} \frac{\partial \bar{v}}{\partial x} - \bar{v} \frac{\partial \bar{v}}{\partial y} \\ &+ \frac{1}{2} K_x \frac{\partial^2 \bar{v}}{\partial x^2} + \frac{1}{2} K_y \frac{\partial^2 \bar{v}}{\partial y^2}\end{aligned}\quad (18)$$

These equations can be solved numerically at a grid of points on the region of interest for a specific set of time-varying boundary conditions. The term \mathbf{v}_a derived in this section has the sole function of transporting the fine-scale (filaments) of the plume. Therefore, the grid point separation Δ is defined to be larger than the scale of the filaments. The advective wind velocity at locations between the grid points is determined by interpolation based on the advective wind at the adjacent grid points. This approach yields a continuous, spatially varying, and time varying model of the advection of the plume elements with a reasonable characterization of the physics. Therefore, the wind velocities at distinct but nearby points are correlated, but spatially varying.

When a sequence of filaments is released at a fixed location, the advection terms $(\bar{u}, \bar{v}, \bar{w})$ generate a meandering trail of filaments, as shown in Fig. 1. This figure depicts a top down view of a 100 by 100 m field. The above equations were solved numerically for boundary conditions generated by a mean flow of $[1, 0] \frac{m}{s}$ plus a colored noise process. The colored noise process at each corner is implemented by filtering unit Gaussian white noise by $H(s) = G \frac{a}{s^2 + bs + a}$. For simulations in which we want to generate large amplitude meander, we typically select $(a, b, G) = (0.04 \frac{rad^2}{s^2}, 0.04 \frac{rad}{s}, 20)$. For simulations in which we want to generate small amplitude meander, we typically select $(a, b, G) = (0.5 \frac{rad^2}{s^2}, 0.1 \frac{rad}{s}, 3)$. The boundary condition along the edge nodes is then generated by interpolating between the values at the two adjacent corners. The components of the model that describe diffusion of the plume elements relative to the plume centerline and the growth of the filaments were turned off for the simulation that generated Fig. 1, so that the figure only shows an instantaneous example of plume centerline meander. Centerline relative filament diffusion and filament growth will be discussed in subsequent sections. The arrows on the figure indicate the instantaneous wind vector at the tail of the arrow. The instantaneous wind vector and the local plume centerline are highly

correlated near the source of the plume. As the distance from the source of the plume increase, the correlation between the directions of these two vectors decreases. The physical explanation of such behavior is that each filament is transported instantaneously along the local wind vector; however, the plume centerline alignment is determined by the entire past history of local wind experienced by all filaments making up the plume.

Implementation of the advective model as described herein yields a spatially and time varying flow field over an area of interest. Transport of odor filaments by this flow field yields a plume centerline with realistic characteristics. In particular, the meandering nature of the plume (with ‘semi-independent’ instantaneous wind direction and plume centerline alignment) is a realistic characteristic of natural plumes [42, 43] and therefore is a significant advancement relative to the wind-tunnel type of puff models used previously for analysis of insect flight response, e.g. see [34, 33]. The finite element model for v_a is not intended to model the small-scale turbulent structure of the wind. Therefore, a relatively large spatial separation (i.e., 5-10 m) of the finite element nodes is reasonable. This large separation allows the approach to be computationally feasible.

2.2. CENTERLINE RELATIVE FILAMENT DIFFUSION

This section describes the model for \mathbf{v}_m . This is the scale of the flow between Δ and the filament size. Assuming that Δ is specified judiciously, this scale of the flow distributes the filaments about the plume centerline. For computational reasons (i.e., the number of nodes increases as $\frac{1}{\Delta^3}$ for three dimensional implementations), this scale of the flow is not modeled through finite difference methods. Instead, the velocity of the i -th filament relative to the centerline \mathbf{v}_{m_i} is modeled as a random process implemented in state-space notation [52] as

$$\dot{\omega} = A \omega + B \nu \quad \mathbf{v}_{m_i} = C \omega + D \nu \quad (19)$$

where $\omega \in \mathbb{R}^n$; A , B , C , and D are appropriately sized matrices; and ν is a white noise process with power spectral density σ_ν^2 (i.e., $\text{cov}(\nu(t), \nu(t + \tau)) = \sigma_\nu^2 \delta(\tau)$ where $\delta(t)$ is the impulse function, see p. 120 in [52] or pp. 81-85 in [53]). The transfer function from ν to \mathbf{v}_{m_i} is

$$\frac{\mathbf{v}_{m_i}}{\nu} = H(s) = C(sI - A)^{-1}B + D \quad (20)$$

where s is the Laplace variable. Therefore, \mathbf{v}_{m_i} is a colored noise process with spectral density defined by

$$PSD_{v_m}(s) = H^*(s)H(s)\sigma_\nu^2 \quad (21)$$

where $H^*(s)$ is the complex conjugate transpose of H .

Note that if the bandwidth of H is large, then $\mathbf{v}_m \approx G\nu$, where $G = H(0)$, so that \mathbf{v}_m is a white noise process. In this case, let \bar{Y} denote the standard deviation of the filament position in the y -direction (i.e., plume width) due only to \mathbf{v}_m (i.e., relative to the centerline). In this case, $\bar{Y} = G\sigma_\nu\sqrt{t}$, where t is the time since the puff was released. This matches Robert's model (see [54] and eqn. (21) in [55]).

Fig. 2 displays an example of the plume generated by the relative diffusion terms \mathbf{v}_{m_i} , when advection is the constant vector $\mathbf{v}_a = [1, 0, 0]$ m/s and filament growth is turned off; therefore, this figure illustrates only the effect of \mathbf{v}_m (i.e., centerline relative diffusion). For this simulation, each component of \mathbf{v}_{m_i} was a white noise process with spectral density given by $\sigma_\nu = 2\frac{m/s}{\sqrt{Hz}}$.

2.3. FILAMENT MODEL AND GROWTH

When summed, \mathbf{v}_{m_i} and \mathbf{v}_a describe the velocity of the filament center as the filament is bodily transported over the field of interest. The pointwise calculation of concentration and changing shape of the filament are the topics of this section. As shown in Fig. 2, the plume is the composition of a large number of advected and dispersed filaments. Given a large number of filaments, the overall instantaneous concentration at $\mathbf{x} = (x, y, z)$ due to all the filaments is just the sum of the concentrations at that location contributed by each filament:

$$C(\mathbf{x}, t) = \sum_{i=1}^N C_i(\mathbf{x}, t) \frac{\text{molecules}}{\text{cm}^3} \quad (22)$$

where N is the number of filaments currently being simulated. Note that this model allows the instantaneous odor concentration to be evaluated at any position and time of interest. This pointwise concentration measurement can be converted into a flux by multiplying by the local wind velocity \mathbf{v}_a and the effective area of the sensor cross-section.

The concentration at location \mathbf{x} due to the i -th filament is modeled as

$$C_i(\mathbf{x}, t) = \frac{Q}{\sqrt{8\pi^3 R_i^3(t)}} \exp\left(\frac{-r_i^2(t)}{R_i^2(t)}\right) \frac{\text{molecules}}{\text{cm}^3 \text{filament}}$$

$$r_i(t) = \|\mathbf{x} - \mathbf{p}_i(t)\| \text{ cm}$$

where Q represents the amount of odor released (i.e., molecules per filament) and R_i is a parameter controlling the size of the i -th filament. This expression is derived based on the assumption that the filament contains material normally distributed relative to the filament center. Therefore, if $C_i(x)$ is integrated over the (infinite) spatial extent of the filament, then it correctly predicts Q molecules in the filament. Therefore, the mass of the odor producing chemical is conserved as the filament size R_i changes.

Various models are available for the time derivative of the radius of the i -th filament. Here, only two models are presented. For the first model, let the radius of the i -th filament be assumed to change as

$$R(t) = (R^{\frac{2}{3}}(0) + \gamma t)^{\frac{3}{2}}$$

then the rate of growth of the i -th filament is

$$\frac{dR}{dt} = \frac{3}{2} \gamma R^{\frac{1}{3}}.$$

Note that the same solution can be obtained with fewer computations by solving

$$\frac{d\rho}{dt} = \gamma$$

and defining $R = \rho^{1.5}$. For the second model, let the radius of the i -th filament be assumed to change as

$$R(t) = (R^2(0) + \gamma t)^{\frac{1}{2}}$$

then the rate of growth of the i -th filament is

$$\frac{dR}{dt} = \frac{\gamma}{2R}.$$

Note that the same solution can be obtained with fewer computations by solving

$$\frac{d\rho}{dt} = \gamma$$

and defining $R = \rho^{\frac{1}{2}}$. These expressions are intended to account for molecular diffusion and growth of the filament due to the smallest length scales of the turbulent flow. Alternative models of filament growth could be combined to account for different regimes of filament growth.

For the simulations presented herein, $\bar{Q} = 8.3 \times 10^9 \frac{\text{molecules}}{\text{s}} = 14 \frac{\text{nanograms}}{\text{hr}}$ for a pheromone with molecular weight 282 $\frac{\text{grams}}{\text{mole}}$, which is the rate of emission of pheromone by a female gypsy moth [56]. The parameter $Q = \frac{\bar{Q}}{n}$ where n is the filament release rate in $\frac{\text{filament}}{\text{s}}$. The filament release

rate is of considerable importance and is a user determined function. All simulations presented herein have $n = 10 \frac{\text{filaments}}{\text{sec}}$. The second model of filament growth is used with $\gamma = 0.001 \frac{m^2}{s}$ and $R^2 = 0.001 m^2$ at the time of release. This initial filament size was selected to be characteristic of the size of the female gypsy moth.

Fig. 3 displays an example of the plume that results when advection, centerline relative diffusion, and filament growth are all active. Again, the local instantaneous wind direction and plume centerline do not necessarily align, except near the source. Fig. 4 displays a typical example of the sensed concentration resulting from the simulated model.

An alternative expression

$$\bar{C}_i(\mathbf{x}) = \frac{Q}{\sqrt{8\pi^3 \det(P)}} \exp\left(-(\mathbf{x} - \mathbf{p}_i)\mathbf{P}^{-1}(\mathbf{x} - \mathbf{p}_i)\right) \frac{\text{molecules}}{\text{cm}^3}. \quad (23)$$

with \mathbf{P} a time varying positive definite matrix would allow both the size and shape of each filament to be altered while maintaining the number of molecules per filament as Q (i.e., conserving the mass of the the odor-producing chemical).

2.4. SENSOR MODEL

The sensed concentration is modeled as a low pass filtered and threshold specified version of the instantaneous concentration,

$$\frac{dc(t)}{dt} = -\alpha c(t) + \alpha C(\mathbf{x}_s(t)) \quad (24)$$

$$y(t) = \begin{cases} c(t) & \text{if } c(t) > \tau \\ 0 & \text{otherwise} \end{cases} \quad (25)$$

where α is the filter bandwidth, τ is the sensor threshold, $c(t)$ is an internal state of the filter, and $\mathbf{x}_s(t)$ is the (possibly time varying) sensor position. The filter input is the instantaneous concentration at the sensor location $C(\mathbf{x}_s(t))$. The filter output is $y(t)$. The effect of the sensor on the downwind plume is not modeled. In the results that follow, α is varied. The threshold τ was selected to match the threshold of male response to pheromone in the gypsy moth (*Lymantria dispar*) which is $4 \times 10^4 \frac{\text{molecules}}{\text{cm}^3}$ [30].

3. Model Analysis

This section presents simulated plume data in various formats (long-term averages, amplitude statistics, temporal statistics). The intent is to present sufficient information to allow verification that the simulated plume has the general characteristics of odor plumes encountered in field experiments. Our main interests in such a validation are the amplitude (i.e., mean versus distance, 'in-plume' mean versus distance, and peak to mean) and short duration temporal statistics (i.e., intermittency, pulse width, and burst return interval). The higher order statistical information is presented for completeness. See the Appendix for definitions of the various statistical quantities.

For analysis relative to field experiments, we compare the simulation results with field measurements presented by Jones in [27]. Jones analyzed experimental data acquired using specially designed instruments with a time resolution of 0.01 s. The data presented by Jones includes plume statistics as a function of sensor bandwidth and distance from the source. This portion of the Jones data is included herein for ease of reference as Tables I and II. In addition, the Jones article contains histograms that present short-term odor statistics (pulse amplitude, burst length, and burst return period) that are directly relevant to the studies motivating the development of this simulation model. Those figures could not be included herein, but they are compared qualitatively with the simulation results in Section 3.3.

3.1. LONG-DURATION TIME AVERAGES

Gaussian models are widely used descriptions for the long-time average concentration. Although our main interest is to replicate in simulation the short-term intermittent structure of plumes, it is also of interest to investigate whether the long-term time average of the simulated plume replicates existing Gaussian models [24].

Fig. 5 plots the 3 minute time-average contour for the simulated plume corresponding to the threshold of $0.04 \times 10^6 \frac{\text{molecules}}{\text{cm}^3}$. Also shown is the Sutton model isopleth, generated from eqn. (1) with $S_y = 0.5C_y x^{2-n/2}$ and $S_z = 0.5C_z x^{2-n/2}$ for the parameters $n=1$, $Q=20$, $C_y=0.4$, and $C_z=0.2$. The 3-minute time-averaged simulation data contour is in close agreement with the Gaussian contour. This is true even though the instantaneous plume has the desired characteristics (i.e., sinuous and intermittent). This fact is highlighted by a direct comparison of Figs. 3 and 5. In

simulated meters, both figures have the same x dimensions. The y-scale of Fig. 3 is twice the scale of Fig. 5. Fig. 3 plots instantaneous concentration as a function of position, whereas Fig. 5 shows the time-average contour. Misuse of Fig. 5 would imply that a sensor placed anywhere within the contour would detect above threshold concentrations. The instantaneous plume ‘snapshot’ of Figs. 3 shows that the above threshold locations are actually localized and time varying.

For clarity of presentation, additional time-averaged simulated plume contours are not included in Fig. 5; however, such contours match additional characteristics of the Gaussian plume model. For example, as the duration of the time-average increases, the width of a given contour increases.

3.2. AMPLITUDE STATISTICS

Statistics⁴ related to the amplitude of the concentration time series are presented in this section. Because the intent of this section is to validate that the simulation data reproduce key characteristics of actual plume data, the form of the data presentation herein is defined to match that of [27]. To facilitate comparison, the tabular data from [27] is included here as Tables I and II. The simulated data used to compute the statistics of this section are from a simulation with an integration time step of 0.01 s and a duration of 10 minutes (i.e., 60000 points). During the simulation, the filament release rate was 10 filaments per second. The simulated data statistics are presented in Tables III and IV.

The first row of data in Table III presents mean sensed concentration as a function of downwind distance ($d = 2, 5, 10$, and 15 meters). As for the Jones data in Table I, the mean concentration decreases as a function of distance from the source. The top graph of Figure 6 plots the mean concentration versus downwind distance from the source for the simulation and Jones data. Because the units are distinct, both sets of data have been normalized to unit magnitude at a downwind distance of 2 m. The decrease of the mean with downwind distance is caused by the width of the plume increasing, each puff becoming wider, and the area over which the plume meanders increasing with distance from the source. As noted in [27], the mean concentration is not affected by filtering of the data.

The second row of data in Table III presents the conditional mean of the simulated plume as a function of downwind distance from the source. This quantity is determined by calculating the mean concentration only when the sensor is in the plume. Note that, as expected based on physical

principles, the conditional mean is larger than the unconditional mean and the conditional mean decreases more slowly than the unconditional mean as a function of source distance. The bottom graph of Figure 6 plots the conditional 'in the plume' mean concentration versus downwind distance from the source for the simulation and Jones data. Again both sets of data have been normalized to unit magnitude at a downwind distance of 2 m.

Table IV presents second through fourth order (non-dimensional) moments and other key parameters of the concentration time series as a function of both downwind distance and filtering bandwidth. The indicated bandwidth is that of a first order low pass filter (20 dB per decade). The data in Table IV is presented in the same format as the Jones data of Table II. Although it is very difficult to match higher order statistics, the general trends of the data in these tables are very similar. The peak-to-mean ratio decreases as the filter bandwidth decreases, because the peak of the filtered quantity is decreased while the mean is unaffected. Also, the peak-to-mean ratio increases with distance, because the mean concentration decreases more rapidly (decreased by filament growth, dispersion about the centerline, and movement of the centerline) than does the peak concentration (decreased by filament growth). Lastly, the intermittency (percent out of the plume) increases with distance, because the meandering of the plume causes the plume to move across a larger area at greater distances from the source.

3.3. TEMPORAL STATISTICS

Temporal statistics related to the concentration time series are analyzed and presented in this section. Again, comparison is made with the experimental statistics presented in [27]. The main temporal statistics that are of interest are the distribution of burst lengths and the distribution of burst return periods, where each of these terms is defined in the appendix. These distributions are presented in Fig. 7 for two downwind distances and for two thresholds. The threshold is important, as it defines when a sensed concentration is counted for constructing the histogram. The dynamic range of the sensor and data in this experiment was $C_s(t) \in [0.04, 10000] \times 10^6 \frac{\text{molecules}}{\text{cm}^3}$.

The histograms correspond well with those of [27]. In both the field and simulation histograms, the burst lengths are significantly shorter than 1.0 s as dictated by the filamentous nature of the real and simulated plumes. As the threshold increases, the number and duration of the bursts decreases. In both the field and simulation data, the burst return distribution appears to be bimodal with

one peak at or below 0.1 s and a second peak at or above 1.0 s. The physical explanation for this is that the sensor may not detect concentrations either due to the sensor being out of the plume or the sensor being between filaments while still 'in the plume.' Meandering of the plume causes the 'out of plume' burst return period to have long duration and to increase with distance from the source. The burst return period between filaments while 'in the plume' has much shorter duration and increases slowly with distance.

4. Conclusions

This article has presented a computationally feasible simulation model suitable for Monte Carlo type analysis of dispersion in a turbulent medium. This tool is particularly important in studies where the critical item of interest is instantaneous concentration rather than time-averaged exposure. The method presented paid particular attention to creating a model with a continuous but time varying plume centerline, dispersion about the centerline, experimentally valid long-term averages, and experimentally validated short duration temporal and amplitude statistics. The model allows calculation of the wind velocity and concentration at any location and at any simulated time step (increments of 0.01 s for the current implementation). The user definable parameters allow the model to be tuned for a wide variety of applications.

To achieve the fast numeric computation required for the batch Monte Carlo simulation analysis of possible plume tracing strategies, the plume simulation did not attempt to model the fine-scale flow characteristics. This simplifying assumption was motivated by the characteristics of the plume tracing application, where the vehicle is expected to have only a low bandwidth (≈ 1 Hz) flow sensor. The simulation was designed to maintain the plume characteristics that significantly complicate the plume tracing problem (meander, intermittency, and varying flow). The simulation therefore provides a challenging environment for evaluation of plume tracing algorithms.

The level of fine-scale resolution that is used by biological entities or that is required for engineered devices to perform plume tracing is still an open issue⁵. For biological entities the answer to this question is a key issue in research focused on identifying how nature solves such problems. For engineered systems, the answer to this question determines, in part, the quality of sensors that will be required. If the task can be solved without detailed analysis of the fine-scale plume

structure, then low performance and hence lower cost sensors can be used. If detailed analysis of the fine scale structure is required, then simulation based performance analysis will require higher fidelity modeling. Some possible directions for improving the simulation include: (1) adapting the sub-gridscale velocity characteristics based on the characteristics of the advective velocity [57, 58]; and, (2) adjusting the characteristics of v_{m_i} as a function of the scale of the puff (i.e., Richardson or scale-dependent dispersion). A key issue related to such improvements will be the tradeoff between increased model fidelity versus increased computation.

5. Acknowledgement

Jay Farrell thanks Akula Venkatram for his help at the onset of this project, especially for the introduction to puff-based modeling approaches. The authors thank Chris Jones for his input to this effort and Dave Thompson for his opinions on an early draft of this manuscript. This research was supported by a grant from the Office of Naval Research (ONR N00014-98-1-0820) under the ONR/DARPA Chemical Plume Tracing Program.

Appendix

A. Parameter Definitions

Tables II and IV presents various statistics of the simulated plume. This appendix defines the presented statistical quantities.

A.1. AMPLITUDE STATISTICS

The concentration $C(\mathbf{p}, t)$ is a time varying function of position. Although the concentration is time varying, we will assume that the statistics of the process are stationary and ergotic. Therefore, ensemble statistics will be calculated based through time integrals.

The mean concentration is defined by

$$\bar{C}(\mathbf{p}) = \frac{1}{T} \int_0^T C(\mathbf{p}, \tau) d\tau. \quad (26)$$

The n-th central moment is defined as

$$\bar{M}_n(\mathbf{p}) = \frac{1}{T} \int_0^T [C(\mathbf{p}, \tau) - \bar{\Gamma}(\mathbf{p})]^n d\tau. \quad (27)$$

For $n=2,3,4$, these moments are the fluctuation variance, skewness, and kurtosis, respectively. To allow direct comparisons between different experiments, it is useful to express the n-th central moment in the non-dimensional form

$$M_n(\mathbf{p}) = \frac{\left(\frac{1}{T} \int_0^T [C(\mathbf{p}, \tau) - \bar{\Gamma}(\mathbf{p})]^n d\tau \right)^{1/n}}{\bar{\Gamma}(\mathbf{p})}. \quad (28)$$

The non-dimensional second moment is referred to as the relative intensity of fluctuations. In Table IV the skewness and kurtosis are expressed in non-dimensional form.

The quantity $\hat{\Gamma}/\bar{\Gamma}$ is the peak to mean ratio. This quantity is calculated herein as the peak over the entire experiment divided by the mean over the entire experiment. This quantity could also be calculated as the average peak height (over all peaks) divided by the mean concentration or as the average peak height (over all peaks) divided by the conditional (i.e., in the plume) mean concentration.

Due to the sinuous nature of the plume, there exist periods of time when the sensor will not be 'in the plume.' Relative to a threshold τ , the *intermittency* I is defined as the percentage of time during the experiment that the sensed concentration was below threshold. The above amplitude statistics can be calculated over the entire duration of the experiment or only during the portion of the experiment when the sensor was in the plume. In this article, only the second row of data in Tables I and III is restricted to times when the sensor was in the plume.

A.2. TEMPORAL STATISTICS

Fig. 4 displays a short segment of the simulated concentration at a position 2 m downwind from the source. The symbol t_{pi} defines the width of the i-th peak (i.e., above threshold τ). The symbol t_{gi} defines the width of the i-th gap (i.e., below threshold τ). The symbol $t_{bi} = t_{pi} + t_{gi}$ defines the time between the start of two consecutive pulses (i.e., pulse return). Note that these time periods and their distribution are threshold dependent. Fig. 4 indicates the peak and gap duration of the first pulse corresponding to a threshold of 2000. Based on these definitions, if n_{pi} and n_{gi} denote

the number of pulses and gaps in the experiment, respectively, then

$$T \approx \sum_{i=1}^{n_{pi}} t_{pi} + \sum_{i=1}^{n_{gi}} t_{gi} \quad (29)$$

where T is the experiment duration and the approximation is only due to the experiment not starting and stopping at the beginning or end of pulses. Fig. 7 displays normalized histograms of the pulse widths (i.e., t_{pi}) and pulse returns (i.e., t_{bi}).

Notes

¹ In the last decade there have been at least three research programs in the United States: the DARPA Dog's Nose Program, the ONR Chemical Sensing in the Marine Environment Program, and the DARPA/ONR Chemical Plume Tracing Program.

² A typical Monte Carlo batch evaluation of a single strategy involves 10,000 (100 repetitions of each starting location from a grid of 100 source relative starting locations.) plume simulations each 300 seconds long. A single plume simulation must be capable of returning at time t the concentration and (low bandwidth) flow velocity at any location within a 100×100 m search area.

³ A few simulation images are contained in this article. The time varying simulation output is more interesting. Therefore, an executable version (for Windows) of the simulation described herein is available for download at <http://www.ee.ucr.edu/~farrell>. The source code in C is available through the first author.

⁴ See appendix for parameter definitions.

⁵ The authors also thank the reviewers for their time and efforts. The ideas of this paragraph were formed based on suggestions from the reviewers.

References

1. Bossert, W. H. and Wilson, E. O.: 1963, The analysis of olfactory communication among animals. *J. Theor. Biol.* **48**, 443-469.
2. Dusenberry, D. B.: 1992, *Sensory Ecology: How Organisms Acquire and Respond to Information*. W.H. Freeman, New York.
3. Vickers, N. J.: 2000, Mechanisms of animal navigation in odor plumes. *Biol. Bull.* **198**, 203-212.
4. Zimmer, R. K. and Butman, C. A.: 2000, Chemical signaling processes in the marine environment. *Biol. Bull.* **198**, 168-187.

5. Hassler, A. D. and Scholz, A. T.: 1983, *Olfactory Imprinting and Homing in Salmon*. Springer-Verlag, New York.
6. Lohmann, K. J.: 1992, How sea turtles navigate. *Sci. Amer.* **266**, 82–88.
7. Nevitt, G. A.: 2000, Olfactory foraging by Antarctic procellariiform seabirds: life at high Reynolds numbers. *Biol. Bull.* **198** 245–253.
8. Atema, J.: 1995, Chemical signals in the marine environment: dispersal, detection, and temporal signal analysis. *Proc. Nat. Acad. Sci. U.S.A.* **92**, 62–66.
9. Basil, J. and Atema, J.: 1994, Lobster orientation in turbulent odor plumes: simultaneous measurements of tracking behavior and temporal odor patterns. *Biol. Bull.* **187**, 272–273.
10. Devine, D. V. and Atema, J.: 1982, Function of chemoreceptor organs in spatial orientation of the lobster, *Homarus americanus*: differences and overlap. *Biol. Bull.* **163**, 144–153.
11. Weissburg, M. J. and Zimmer-Faust, R. K.: 1994, Odor plumes and how blue crabs use them in finding prey. *J. Exp. Biol.* **197**, 349–375.
12. Cardé, R.T.: 1996, Odour plumes and odour-mediated flight in insects. In: *Olfaction in Mosquito-Host Interactions*, pp. 54–70. CIBA Found. Symp. 200: John Wiley & Sons.
13. Cardé, R.T. and Mafra-Neto, A.: 1996, Mechanisms of flight of male moths to pheromone. In: R.T. Cardé and A.K. Minks (eds.), *Insect Pheromone Research. New Directions*, pp. 275–290, Chapman and Hall, New York.
14. Mafra-Neto, A. and Cardé, R. T.: 1994, Fine-scale structure of pheromone plumes modulates upwind orientation of flying moths. *Nature* **369**, 142–144.
15. Grasso, F. W.: 2001, Invertebrate-inspired sensory-motor systems and autonomous, olfactory-guided exploration. *Biol. Bull.* **200**, 160–168.
16. Arbas, E. A., Willis, M. A. and Kanzaki, R.: 1993, Organization of goal-oriented locomotion: pheromone-modulated flight behavior of moths. In: Beer, R. D., Ritzmann, R.E., McKenna, T., (eds.), *Biological Neural Networks in Invertebrate Neuroethology and Robotics*, pp. 159–198, Academic Press, San Diego.
17. Baker, T. C. and Vickers, N. J.: 1996, Pheromone-mediated flight in moths. In: R.T. Cardé and A.K. Minks (eds.), *Insect Pheromone Research. New Directions*, pp. 248–264, Chapman and Hall, New York.
18. Kaissling, K.-E.: 1997, Pheromone-controlled anemotaxis in moths. In Lehrer, M. (ed.) *Orientation and Communication in Arthropods*, pp. 343–374, Birkhäuser Verlag, Basel.
19. Willis, M. A. and Arbas, E. A.: 1996, Active behavior and reflexive responses: Another perspective on odor-modulated locomotion. In: R.T. Cardé and A.K. Minks (eds.), *Insect Pheromone Research. New Directions*, pp. 304–319, Chapman and Hall, New York.
20. Witzgall, P.: 1996, Modulation of pheromone-mediated flight in male moths. In: R.T. Cardé and A.K. Minks (eds.), *Insect Pheromone Research. New Directions*, pp. 265–274, Chapman and Hall, New York.
21. Gifford, F. A.: 1960, Peak to average concentration ratios according to a fluctuating plume dispersion model. *Int. J. Air Poll.* **3**, 253–260.
22. Gifford, F. A.: 1968, An outline of theories of diffusion in the lower layers of the atmosphere. In: D. H. Slade (ed.), *Meteorology and Atomic Energy*, pp. 65–116, US Atomic Energy Comm..

23. Sutton, O. G.: 1947, The problem of diffusion in the lower atmosphere. *Quart. J. Roy. Meteorol. Soc.*, **73**, 257-281.
24. Sutton, O. G.: 1953, *Micrometeorology*, McGraw-Hill, New York.
25. Briggs, G. A.: 1973, Diffusion estimation for small emissions, ATDL Contributions File No. (Draft) 79, Air Resources Atmospheric Turbulence and Diffusion Laboratory, NOAA, Oak Ridge, Tennessee.
26. Griffiths, R. F.: 1994, Errors in the use of the Briggs parameterization for atmospheric dispersion coefficients. *Atmos. Environ.* **28**, 2861-2865.
27. Jones, C. D.: 1983, On the structure of instantaneous plumes in the atmosphere. *J. Hazardous Mater.*, **7**, 87-112.
28. Murlis, J., Elkinton, J. S. and Cardé, R. T.: 1992, Odor plumes and how insects use them. *Annu. Rev. Entom.* **37**, 505-532.
29. Thomas, M. D.: 1961, Effects of air pollution on plants. *Air Pollution*, p. 442, Columbia University Press, New York.
30. Elkinton, J. S., Cardé and R. T., Mason, C. J.: 1984, Evaluation of time-average dispersion models for estimating pheromone concentration in a deciduous forest. *J. Chem. Ecol.* **10**, 1081-1108.
31. Metais, O.: 1997, Numerical simulation of geophysical turbulence and eddies. In: R. L. Dewar and R. W. Griffiths (eds.), *Two-Dimensional Turbulence in Plasmas and Fluids*, pp. 37-63, American Institute of Physics.
32. Terracol, M., Sagaut, P. and Basdevant, C.: 2001, A multilevel algorithm for large-eddy simulation of turbulent compressible flows. *J. Comp. Physics* **167**, 439-474.
33. Belanger, J. H. and Willis, M. A.: 1996, Adaptive Control of Odor-Guided Locomotion: Behavioral Flexibility as an Antidote to Environmental Unpredictability, *Adaptive Behavior*, **4**, 217-253.
34. Belanger J. H. and Arbas, E. A.: 1998, Behavioral strategies underlying pheromone-modulated flight in moths: lessons from simulation studies. *J. Comp. Physiol. A* **183**, 345-360.
35. Byers, J. A.: 1996, Temporal clumping of bark beetle arrival at phermone traps: modeling anemotaxis in chaotic plumes. *J. Chem. Ecol.* **22**, 2133-2155.
36. Byers, J. A.: 1999, Effects of attraction radius and flight paths on catch of scolytid beetles dispersing outward through rings of pheromone traps. *J. Chem. Ecol.* **25**, 985-1005.
37. Egan, B. A. and Mahoney, J. R.: 1972, Numerical modeling of advection and diffusion of urban source pollutants. *J. Appl. Meteorol.* **11**, 312-322.
38. Nadaoka, K., Nihei, Y. and Yagi, H.: 1999, Grid-averaged Lagrangian LES model for multiphase turbulent flow. *International J. Multiphase Flow* **25**, 1619-1643.
39. Pielke, R. A.: 1994, *Mesoscale Meteorological Modeling*, Academic Press, San Diego.
40. Saiki, E. M., Moeng, C.-H. and Sullivan, P. P.: 2000, Large-Eddy simulation of the stably stratified planetary boundary layer. *Bound.-Layer Meteorol.* **95**, 1-30.
41. Sykes, R. I. and Henn, D. S.: 1992, Large-eddy simulation of concentration fluctuations in a dispersing plume. *Atmos. Environ.*, **26A** 3127-3144.
42. Elkinton, J. S., Schal, C., Ono, T. and Cardé, R. T.: 1987, Pheromone puff trajectory and upwind flight of male gypsy moths in a forest. *Physiol. Entomol.* **12**, 399-406.

43. Brady, J. H., Gibson, G. and Packer, M. J.: 1989, Odour movement, wind direction, and the problem of host finding by tsetse flies. *Physiol. Entomol.* **14**, 369–380.

44. Rumbo, R. and Kaissling, K.-E.: 1989, Temporal resolution of odour pulses by three types of pheromone receptor cells in *Antherea polyphemus*. *J. Comp. Physiol. A.* **165**, 281–291.

45. Mafra-Neto, A. and Cardé, R. T.: 1996, Dissection of the pheromone-modulated flight of moths using the single-pulse response as a template. *Experientia* **52**, 373–379.

46. Aylor, D. E., Parlange, J.-Y. and Granett, J.: 1976, Turbulent dispersion of disparlure in the forest and male gypsy moth response. *Environ. Entomol.* **5**, 1026–1032.

47. Aylor, D. E.: 1976, Estimating peak concentrations of pheromones in the forest. In: J. F. Anderson and M. K. Kaya (eds.), *Perspectives in Forest Entomology*, 177–188. Academic Press.

48. Mylne, K. R.: 1992, Concentration fluctuation measurements in a plume dispersing in a stable surface layer. *Bound.-Layer Meteorol.* **60**, 15–48.

49. Anonymous: 1968, Meteorological fundamentals for atmospheric transport and diffusion studies. In: D. H. Slade, (ed.), *Meteorology and Atomic Energy*, pp. 13–63, U.S. Atomic Energy Commission.

50. Stacey, M. T., Cowen, E. A., Powell, T. M., Dobbins, E., Monismith, S. G. and Koseff, J. R.: 2000, Plume dispersion in a stratified, near-coastal flow: measurements and modeling. *Continental Shelf Res.* **20**, 637–663.

51. Pasquill, F. and Smith, F.B.: 1983, *Atmospheric Diffusion*, 3rd ed., Halsted Press, New York.

52. Luenberger, D. G.: 1979, *Introduction to Dynamic Systems*, John Wiley, New York.

53. Jazwinski, A. H.: 1970, *Stochastic Processes and Filtering Theory*, Academic Press, San Diego.

54. Roberts, O. F. T.: 1923, The theoretical scattering of smoke in a turbulent atmosphere. *Proc. Roy. Soc. A* **104**, 640–654.

55. Gifford, F. A.: 1959, Statistical properties of a fluctuating plume dispersion model. In: F. N. Frankiel and R. A. Shepard (eds.), *Advances in Geophysics*, Vol. 6, *Atmospheric Diffusion and Air Pollution*, p. 117, Academic Press, New York.

56. Tang, J.D., Charlton, R. E., Cardé, R. T., and Yin, C.-M.: 1992, Diel periodicity and influence of age and mating on sex pheromone titer in gypsy moth, *Lymantria dispar*. *J. Chem. Ecol.* **18**, 749–760.

57. Moin, P., Squires, K., Cabot, W. and Lee, S.: 1991, A dynamic subgrid-scale model for compressible turbulence and scalar transport, *Phys. Fluids A* **3**, 2746–2757.

58. Germano, M., Piomelli, U., Moin, P., and Cabot, W. H.: 1991, A dynamic subgrid-scale eddy viscosity model, *Phys. Fluids, A* **3**, 1760–1765.

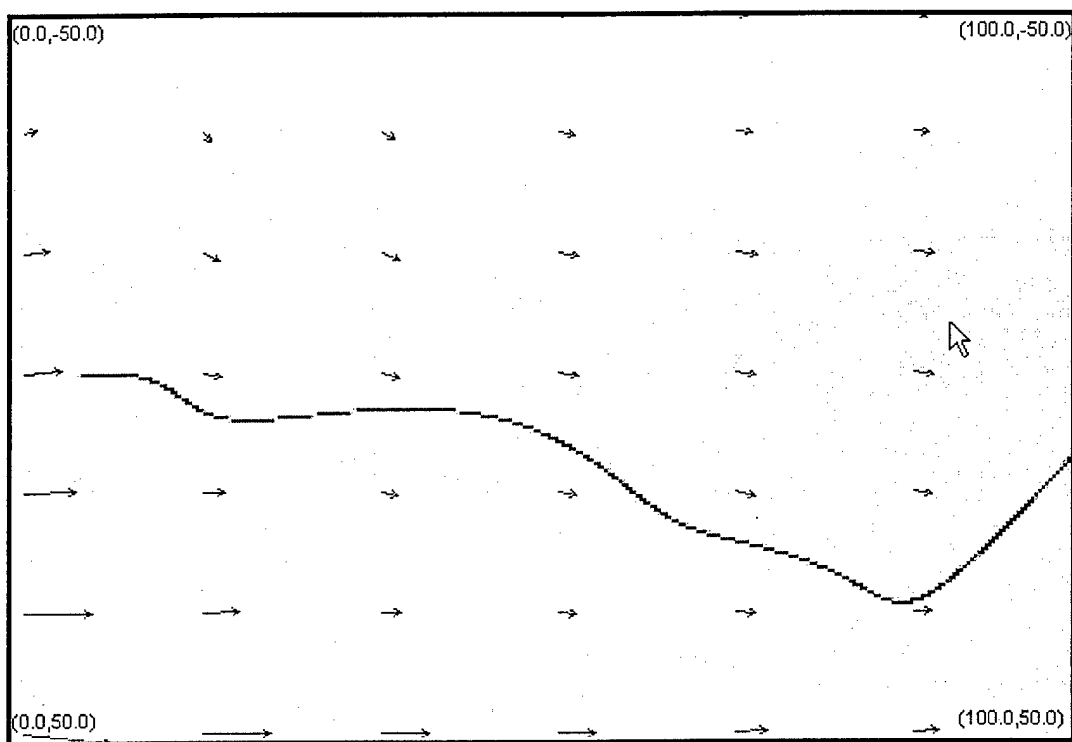


Figure 1. Plume due only to the advection term v_a . The area represented is 100 by 100 m with the odor source at $(x, y) = (5, 0)$ m. Each arrow indicates the local wind vector at the tail of the arrow. The meandering of the plume centerline is due to advection of a sequence of odor filaments by the local wind.

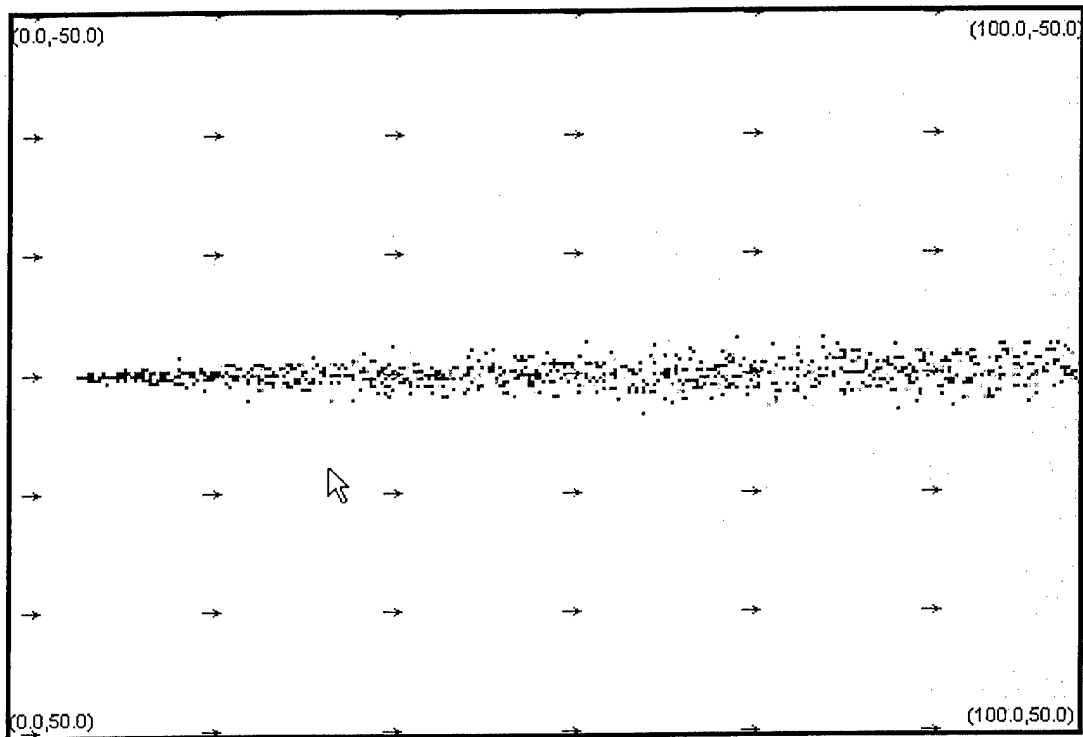


Figure 2. Plume growth due only to relative diffusion with constant advection (i.e., $\mathbf{v}_a = [1, 0, 0] \frac{m}{s}$). The area represented is 100 by 100 m with the odor source at $(x, y) = (5, 0) m$. Each arrow indicates the local wind vector at the tail of the arrow. The centerline of the instantaneous plume does not meander because the wind is constant.

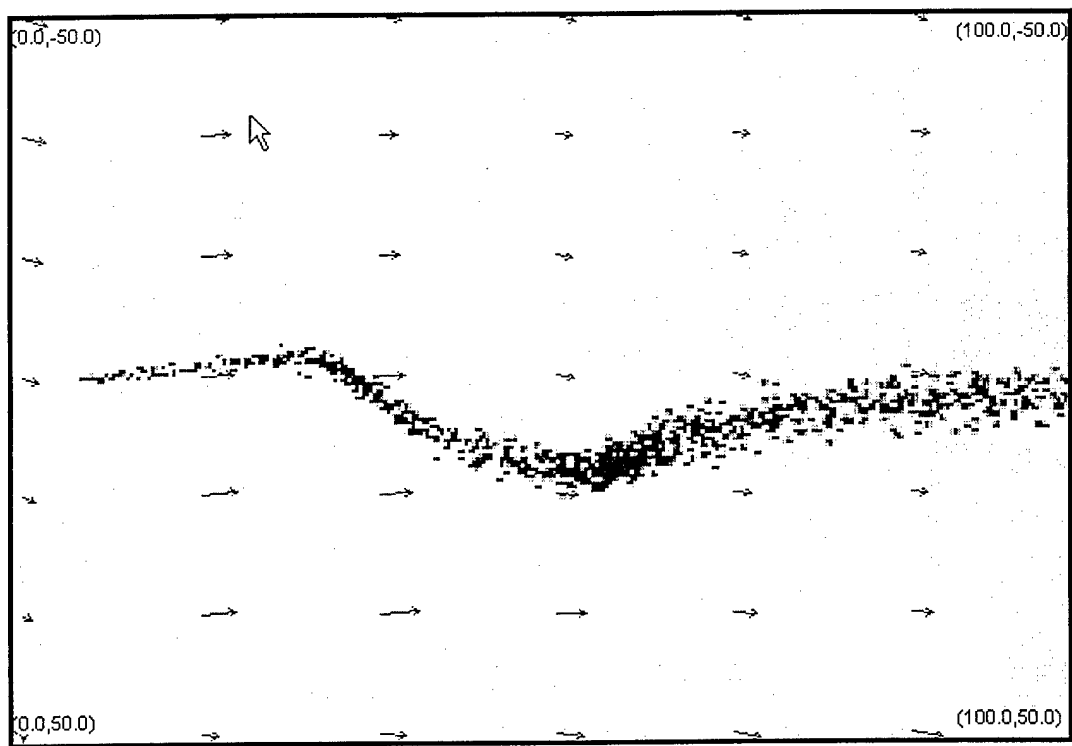


Figure 3. Meandering plume with centerline relative diffusion and filament growth. The area represented is 100 by 100 m with the odor source at $(x, y) = (5, 0)$ m. Each arrow indicates the local wind vector at the tail of the arrow.

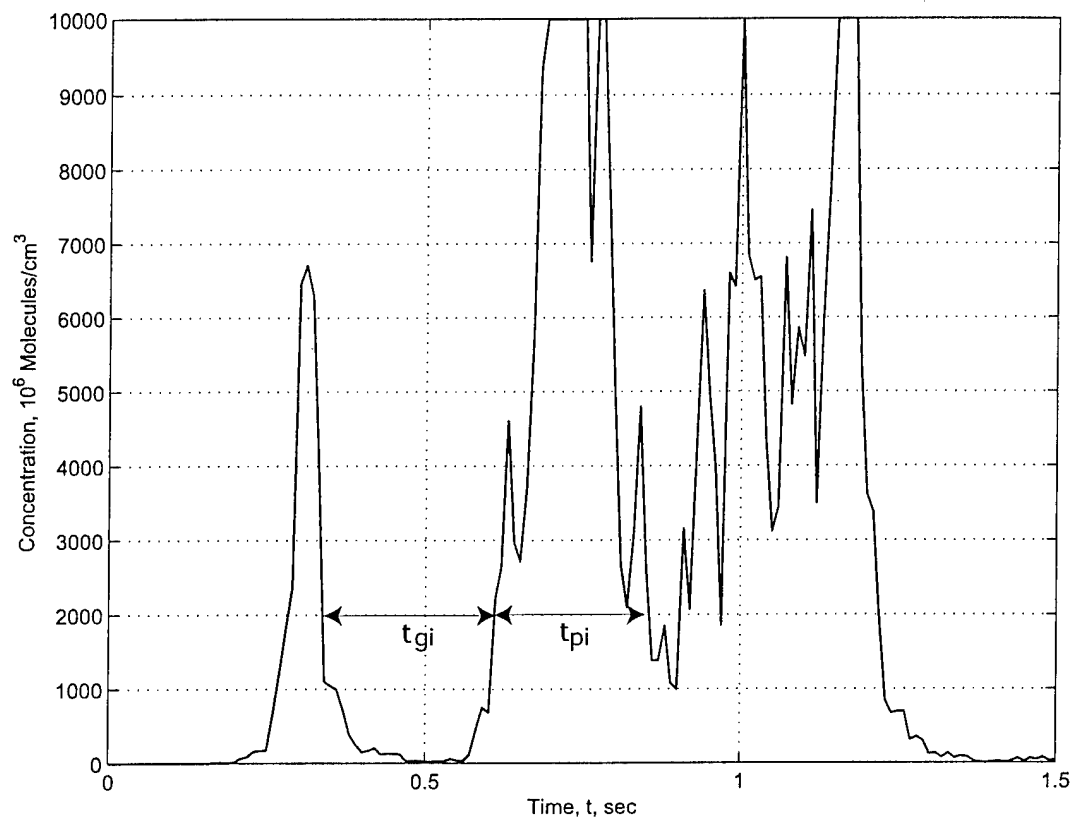


Figure 4. Concentration time series 2 m downwind from the source. The time resolution is 0.01 sec. Release rate is 3 puffs/sec. The concentration is expressed in $10^6 \frac{\text{molecules}}{\text{cm}^3}$.

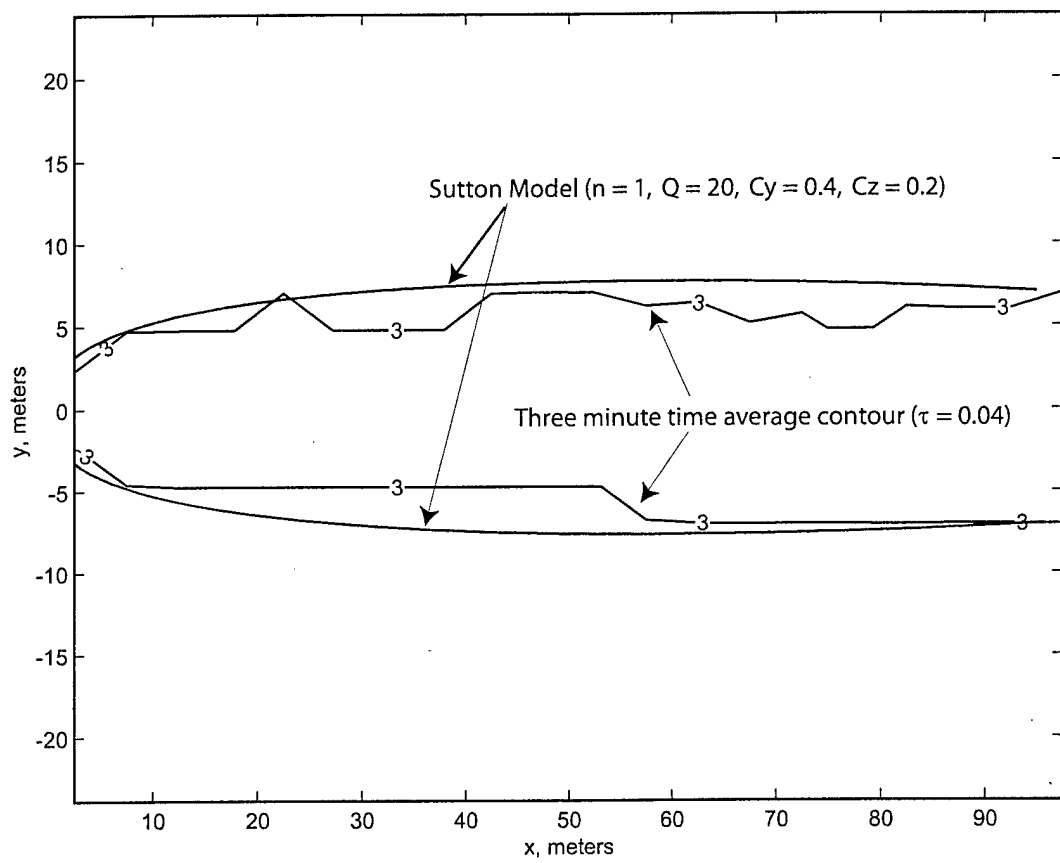


Figure 5. Contour plots for Sutton model and a three minute average of the simulated sensed concentration.

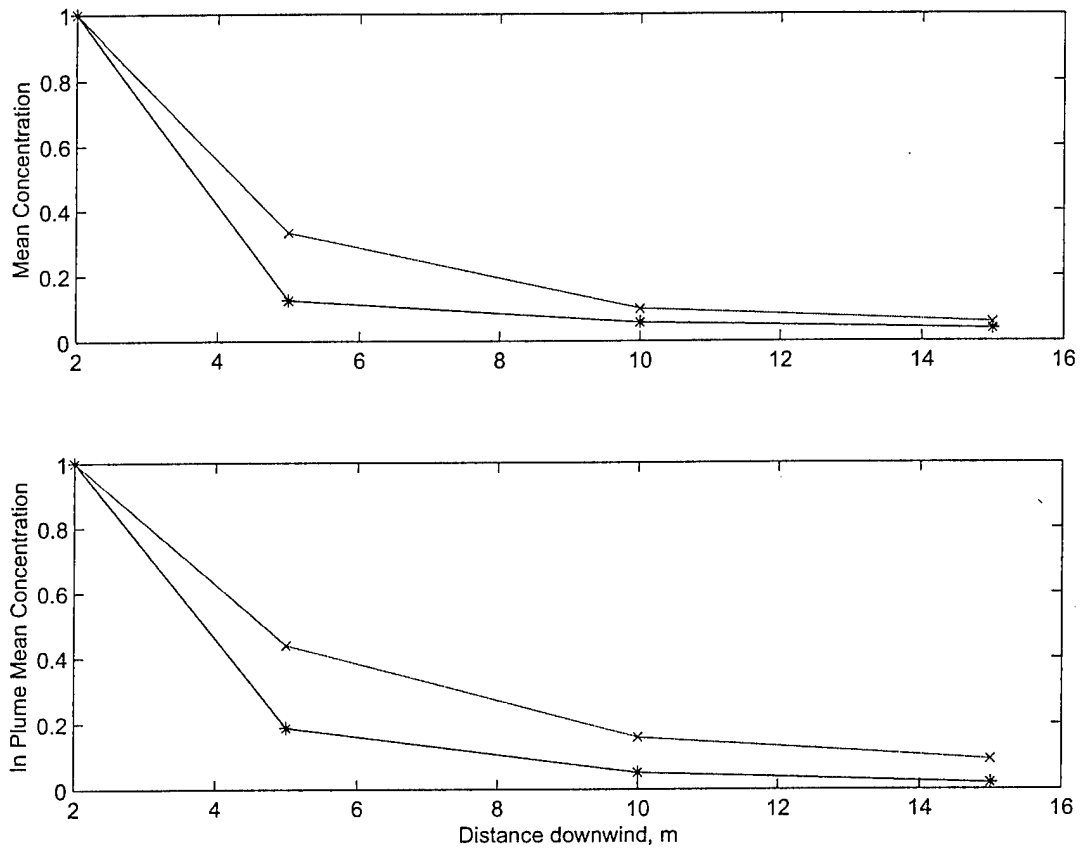


Figure 6. Plots comparing the mean concentration and 'in plume' mean concentration data between simulation (solid with 'x') and field data from [27] (solid with '*'). The actual data contained in Tables I and III has been normalized by their values at 2.0 m.

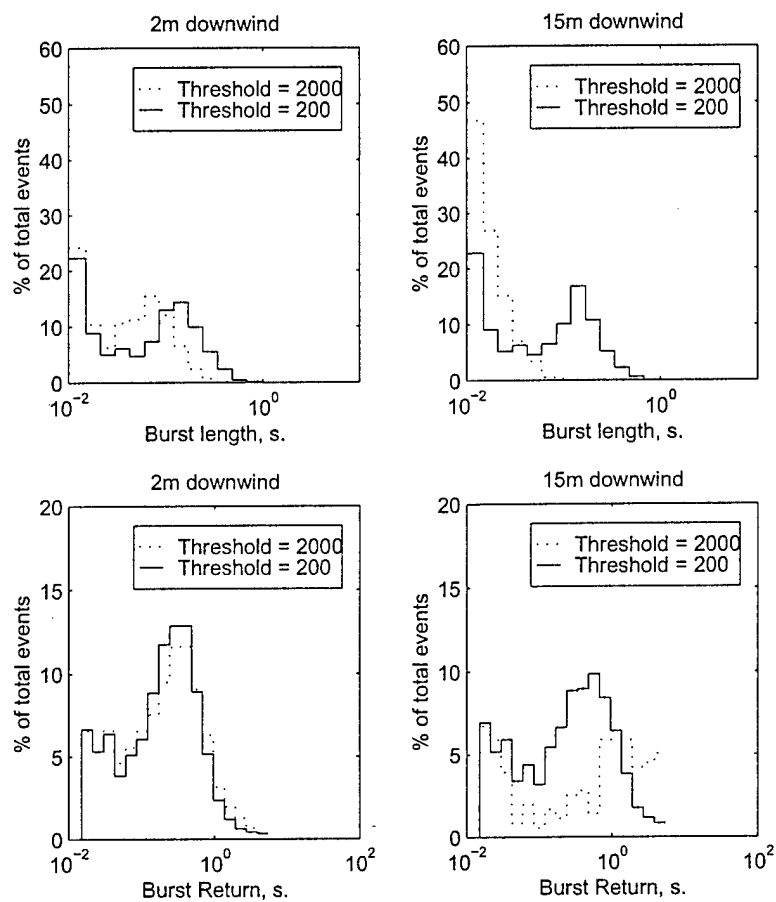


Figure 7. Top left—Burst length distributions for a stationary sensor located 2 m downwind from the source. Top right—Burst length distributions for a stationary sensor located 15 m downwind from the source. Bottom left—Burst return period distributions for a stationary sensor located 2 m downwind from the source. Bottom right—Burst return period distributions for a stationary sensor located 15 m downwind from the source. Compare with Figs. 6 and 7 in [27].

Table I. Data from [27]. The mean over all data is presented in the top data line. The conditional mean for 'in the plume data' is presented in the second data line.

Downwind distance (m)	2	5	10	15
Mean Concentration, $\bar{\Gamma} \left(\frac{nC}{m^3} \right)$	4.21	0.525	0.239	0.159
Conditional Mean Concentration, $\bar{\Gamma}$	28.4	5.33	1.46	0.549

Table II. Data from [27]. Plume data statistics as a function of downwind distance and sensor bandwidth. Processed data for 2 m downwind is presented in the first five data rows. Processed data for 5 m downwind is presented in the second five data rows. Processed data for 10 m downwind is presented in the final five data rows. Skewness and kurtosis are expressed in non-dimensional form.

Name	Symbol	Unfiltered	With low- pass filtering				
			30 Hz	10 Hz	3 Hz	1 Hz	0.3 Hz
Standard deviation	$\sigma_\Gamma, \frac{nC}{m^3}$	12.6	11.0	8.71	5.60	3.77	2.40
Skewness	S_Γ	4.95	4.87	4.62	4.31	4.18	3.93
Kurtosis	K_Γ	30.2	29.6	27.6	25.5	23.2	21.5
Peak to mean ratio	$\hat{\Gamma}/\bar{\Gamma}$	36.4	31.9	25.6	18.4	13.9	6.74
Intermittency	$I(\%)$	85.2	82.7	80.9	78.8	79.1	86.5
Standard deviation	$\sigma_\Gamma, \frac{nC}{m^3}$	2.21	2.08	1.83	1.39	1.03	0.722
Skewness	S_Γ	7.18	6.46	6.27	5.47	4.24	3.29
Kurtosis	K_Γ	66.6	53.3	51.4	39.3	23.7	13.0
Peak to mean ratio	$\hat{\Gamma}/\bar{\Gamma}$	78.2	62.7	58.9	43.3	22.2	10.6
Intermittency	$I(\%)$	90.1	87.9	82.6	84.8	81.0	82.9
Standard deviation	$\sigma_\Gamma, \frac{nC}{m^3}$	0.818	0.765	0.679	0.536	0.395	0.279
Skewness	S_Γ	8.82	7.82	7.48	5.62	4.49	3.50
Kurtosis	K_Γ	129	97.0	89.8	47.0	30.6	14.9
Peak to mean ratio	$\hat{\Gamma}/\bar{\Gamma}$	112	90.4	79.0	48.0	28.5	12.2
Intermittency	$I(\%)$	83.7	83.9	85.2	83.7	83.7	85.2

Table III. Mean concentration of simulation data over 10 minutes (60000 time samples) as a function of distance from the source (unfiltered data). The mean over all data is presented in the top data line. The conditional mean for 'in the plume data' is presented in the second data line. This table is compared with the field data of Table I in Fig. 6.

Downwind distance (m)	2	5	10	15
Mean Concentration, $\bar{\Gamma}$ ($M \frac{molecules}{cm^3}$)	698.01	232.22	69.38	40.48
Conditional Mean Concentration, $\bar{\Gamma}$	1494.0	655.4	237.3	136.9

Table IV. Simulated plume data statistics as a function of downwind distance and sensor bandwidth. Processed data for 2 m downwind is presented in the first six data rows. Processed data for 5 m downwind is presented in the second six data rows. Processed data for 10 m downwind is presented in the final six data rows. Ten minutes (60000 samples) of data. Compare with field data of [27] that is contained in Table II. Skewness and kurtosis are expressed in non-dimensional form.

Name	Symbol	Unfiltered	With low- pass filtering				
			30 Hz	10 Hz	3 Hz	1 Hz	0.3 Hz
Standard deviation	$\sigma_\Gamma, M \frac{molec.}{cm^3}$	2064	2037	1923	1608	1206	873
Skewness	S_Γ	4.53	4.45	4.14	3.36	2.32	1.52
Kurtosis	K_Γ	5.81	5.70	5.29	4.21	2.89	1.80
Peak to mean ratio	$\hat{\Gamma}/\bar{\Gamma}$	14.33	14.33	14.33	14.03	11.76	7.49
Intermittency	$I(\%)$	53.28	52.58	48.54	38.27	28.11	13.15
Relative intensity	γ_Γ	2.96	2.92	2.76	2.30	1.73	1.25
Standard deviation	$\sigma_\Gamma, M \frac{molec.}{cm^3}$	958	944	889	750	570	411
Skewness	S_Γ	7.75	7.57	6.90	5.47	3.80	2.46
Kurtosis	K_Γ	11.20	10.88	9.78	7.54	5.08	3.15
Peak to mean ratio	$\hat{\Gamma}/\bar{\Gamma}$	43.06	43.06	42.59	36.63	23.58	13.73
Intermittency	$I(\%)$	64.57	64.38	63.00	56.84	47.56	28.70
Relative intensity	γ_Γ	4.13	4.07	3.83	3.23	2.46	1.77
Standard deviation	$\sigma_\Gamma, M \frac{molec.}{cm^3}$	339	333	312	265	204	148
Skewness	S_Γ	11.13	10.66	9.40	7.30	5.02	3.15
Kurtosis	K_Γ	18.82	17.76	15.07	11.13	7.21	4.17
Peak to mean ratio	$\hat{\Gamma}/\bar{\Gamma}$	144.14	143.88	130.83	81.64	46.86	20.33
Intermittency	$I(\%)$	70.76	70.70	70.17	66.49	59.54	42.30
Relative intensity	γ_Γ	4.90	4.80	4.50	3.82	2.95	2.14